



This is a repository copy of *Experimental study of cold-formed steel built-up beams*.

White Rose Research Online URL for this paper:
<http://eprints.whiterose.ac.uk/160932/>

Version: Accepted Version

Article:

Meza, F.J., Becque, J. and Hajirasouliha, I. orcid.org/0000-0003-2597-8200 (2020)
Experimental study of cold-formed steel built-up beams. *Journal of Structural Engineering*,
146 (7). 04020126. ISSN 0733-9445

[https://doi.org/10.1061/\(asce\)st.1943-541x.0002677](https://doi.org/10.1061/(asce)st.1943-541x.0002677)

This material may be downloaded for personal use only. Any other use requires prior permission of the American Society of Civil Engineers. This material may be found at [https://doi.org/10.1061/\(ASCE\)ST.1943-541X.0002677](https://doi.org/10.1061/(ASCE)ST.1943-541X.0002677)

Reuse

Items deposited in White Rose Research Online are protected by copyright, with all rights reserved unless indicated otherwise. They may be downloaded and/or printed for private study, or other acts as permitted by national copyright laws. The publisher or other rights holders may allow further reproduction and re-use of the full text version. This is indicated by the licence information on the White Rose Research Online record for the item.

Takedown

If you consider content in White Rose Research Online to be in breach of UK law, please notify us by emailing eprints@whiterose.ac.uk including the URL of the record and the reason for the withdrawal request.



eprints@whiterose.ac.uk
<https://eprints.whiterose.ac.uk/>

EXPERIMENTAL STUDY OF COLD-FORMED STEEL BUILT-UP BEAMS

Francisco J. Meza, Jurgen Becque and Iman Hajirasouliha

Abstract: This paper describes a comprehensive experimental program on cold-formed steel built-up beams with two different cross-sectional geometries. The work aimed to experimentally investigate the interaction between the individual components under increasing loading and to quantify the effect of the connector spacing on the cross-sectional moment capacity and the behaviour of the beams. In total, 12 specimens were tested in a four-point bending configuration, with lateral restraints provided at the loading points in order to avoid global instabilities. The built-up specimens were composed of three or four plain channels with nominal thicknesses of 1.2 mm and 1.5 mm, which were joined together using M6 bolts. Each built-up geometry was tested with three different connector spacings. The specimens were designed to fail by local buckling of their components. Additionally, strut buckling of the channel comprising the top flange in between connector points was observed. The local buckling deformations and the beam deflections were recorded during the tests. The material properties of the test specimens were determined by means of coupon tests and the geometric imperfections were measured prior to testing. The experimental results showed clear evidence of interaction between the local buckling patterns of the components, with the interaction being affected by the connector spacing and the type of geometry. However, the connector spacing showed a less significant effect on the ultimate capacity when failure was governed by local instabilities of the components.

Keywords: Built-up column; Experiment; Cold-formed steel; Stability; Buckling; Imperfection measurements.

Dr. Francisco Meza, F.Meza@steel-sci.com The Steel Construction Institute, Silwood Park, Ascot, SL5 7QN, UK.

Dr. Jurgen Becque, j.becque@sheffield.ac.uk, The University of Sheffield, Sir Frederic Mappin Building, Mappin Street, Sheffield, S1 3JD, UK.

Dr. Iman Hajirasouliha, i.hajirasouliha@sheffield.ac.uk, The University of Sheffield, Sir Frederic Mappin Building, Mappin Street, Sheffield, S1 3JD, UK.

1. Introduction

The use of cold-formed steel (CFS) load-bearing members has become increasingly popular during the past few decades. In many countries, particularly the US, common instances can be found of multi-storey commercial and residential buildings which are entirely constructed out of CFS, while CFS portal frames are finding popular application throughout the world in industrial and agricultural buildings. This evolution can be attributed to the numerous advantages CFS has on offer, such as high strength-to-weight and stiffness-to-weight ratios, convenient handling, transportation and stacking, and a high construction speed, especially when combined with a modular approach. However, due to their reduced wall thickness the ultimate capacity of CFS members is often governed by cross-sectional instabilities such as local and distortional buckling, which may occur in combination with global buckling.

The increasing structural demands on CFS members which ensue from their frequent use as primary structural members are fundamentally at odds with the inevitable limitations on their wall thickness resulting from the fabrication process. Therefore, built-up members are a common solution in current practice when individual sections are not able to carry the load or cover the required span. In structural framing systems this may be the case when large openings are needed in walls for windows or doors, or in floors (e.g. for stairwells). Moreover, in light-weight portal frames the rafters and columns are typically fabricated by connecting two channel sections back-to-back to achieve a doubly symmetric cross-section with increased capacity (Lim and Nethercot, 2002; Dubina et al., 2009; Zhang and Rasmussen, 2014; Blum and Rasmussen, 2019). An added advantage of using built-up sections is that, in principle, they can be assembled on site and therefore the benefits associated with their light weight and ease of handling largely remain.

However, a lack of fundamental understanding of the behaviour of built-up members, as well as the absence of sufficient design guidance in the current design codes (e.g. AISI, 2016;

CEN, 2005) often lead designers to use overly conservative assumptions, which prevents the exploitation of the real potential of these types of sections. Eurocode 3 (CEN, 2005) in particular provides no specific design rules for CFS built-up members. In the North American Specification (AISI, 2016) the provisions for built-up flexural members only apply to I-shaped sections assembled from channels connected through their webs in a back-to-back configuration. These provisions focus on limiting the maximum longitudinal connector spacing to prevent excessive distortion of the components between connectors and avoid tensile failure of the connectors resulting from the tendency of the individual channels to rotate about their shear centre as the load is applied in the contact plane between the webs.

Limited research has been dedicated to built-up CFS flexural members. Wang and Young (2015) experimentally investigated the flexural behaviour of built-up CFS members with open and closed cross-sectional geometries and with circular web holes, with the aim of extending the Direct Strength Method (DSM) to cover these types of members. The open geometry consisted of two lipped channels screw connected in a back-to-back configuration, while the closed cross-section was assembled from two plain channels screwed together through their flanges. The authors explored different ways of calculating the elastic buckling stresses required as input to the DSM, in order to account for the effects of the connectors and the web openings. This research was further extended by the same researchers (Wang and Young, 2016a, 2016b) by carrying out an experimental and numerical investigation of flexural members with four different built-up cross-sectional geometries failing by cross-sectional instabilities. Each built-up geometry was assembled from two identical sections, screw connected either in a back-to-back configuration to form an open section, or through the flanges to form a closed section. The authors assumed in their elastic stability analysis that the built-up geometries behaved as one solid cross-section and found that, while for some built-up geometries the DSM provided acceptable predictions, for others the predictions were

either overly conservative or unsafe. They resolved to modify the DSM equations and proposed tailored equations for each built-up geometry based on their experimental and numerical data. More recently, a study on the flexural rigidity of built-up beams assembled from lipped channels connected back-to-back was presented by Dang and Rasmussen (2018). The authors demonstrated experimentally, numerically and analytically that the flexural rigidity of a built-up beam increases when more intermediate rows of connectors are provided and the connector stiffness increases, particularly when the connectors are located towards the end of the member.

Other research on CFS built-up flexural members has spurred some noteworthy innovations. The built-up LiteSteel beam (LSB), consisting of two channels with hollow rectangular flanges connected back-to-back, was investigated numerically and experimentally by Jeyaragan and Mahendran (2008a, 2008b). The authors found that the detrimental effect of lateral-distortional buckling, to which a single LSB is susceptible, can be mitigated by connecting two LSB back-to-back, resulting in a moment capacity which is more than twice the capacity of the individual LSB section. The Modular Light-Weight Cold-Formed beam (MLC beam) is another innovative built-up beam, consisting of two lipped channels with hollow flanges and a web containing stiffened openings. The channels are laser welded together in a back-to-back configuration with reinforcing plates placed inside the flanges. The MLC beam was designed to provide a high resistance to lateral-torsional buckling and has been extensively investigated both numerically and experimentally (Di Lorenzo et al., 2004, 2006; Landolfo et al., 2009, 2008; Portioli et al., 2012).

This paper presents the results of a detailed experimental programme consisting of 12 CFS built-up beams with two different cross-sectional geometries. The specimens were constructed by joining either three or four plain channel sections together using M6 bolts. The specimens were tested in a four-point bending configuration and were designed to fail by

local buckling of the components within the constant-moment span. Each built-up geometry was tested with three different connector spacings and each test was repeated. The program sought to investigate the various cross-sectional instabilities in the beams, the interaction between the cross-sectional components during buckling and the effect of the connector spacing on the buckling modes and the ultimate capacity of the built-up beams. This experimental work fits within a wider programme investigating CFS built-up members, which also includes CFS built-up column tests (Meza et al. 2016, 2019), with the eventual goal of developing practical design rules for these types of structural members.

2. Specimen geometry

The two different cross-sectional geometries considered in this experimental programme are illustrated in Fig. 1. The first geometry was chosen because it resembles the traditional I-shaped cross-section widely used for beams. Based on the commonly encountered back-to-back channel arrangement, this built-up geometry included two additional channels to increase the flange area and provide improved bending efficiency. The second built-up geometry was selected in consultation with CFS manufacturers/contractors, who pointed out that this built-up geometry is regularly used as a solution to bridge large openings in structural framing systems made of CFS. The back-to-back channels thereby work as a lintel, while the top channel is used as a track to receive the studs of the wall above the opening. Due to the lack of design guidance, however, only the capacity of the back-to-back channels is currently counted on in practice.

The channels were manufactured from pre-galvanized steel plate of grade S450 according to CEN (2016), which has a nominal yield stress of 450 MPa, and with a 0.04 mm Z275 zinc coating applied to both sides, in accordance with CEN (2004). The nominal dimensions of the cross-sections are listed in Table 1. The symbols in the table refer to the dimensions of the individual channels, as clarified in Fig. 2. All beams had a total length of 3400 mm, with a

nominal distance between the end supports of 3000 mm. The specimens were loaded in a four-point bending configuration. The constant moment span, corresponding to the distance between the loading points, had a length of 1600 mm. The portions of the beam between the end supports and the loading points, further referred to as the shear spans, had a length of 700 mm. The built-up specimens were designed with either zero, two or three equally spaced rows of connectors along the constant moment span, in addition to the connectors placed in the cross-sections under the loading points. A close connector spacing along the shear spans of 100 mm was maintained in all test specimens, as shown in Fig. 3, in order to promote load sharing between all components, as well as to avoid failure outside the constant moment region. Two identical beams were fabricated for each configuration in order to gain increased confidence in the results.

A labelling system was used for both the individual components of the cross-section (as indicated in Fig. 1) and the test specimens. The latter consisted of a 'B', followed by a '1' or a '2' to indicate the cross-sectional configuration (with reference to Fig. 1), the number of intermediate rows of connectors between the loading points and the letter 'a' or 'b' to differentiate between the first and the second of twin test specimens. The actual cross-sectional dimensions of each component were measured at several locations along the length before assembly. The dimensions of the web and the flanges were measured using a digital Vernier caliper with a precision of ± 0.03 mm. All measurements were taken of the outside dimensions. The thickness of the cross-section was measured with a micrometre with a precision of ± 0.002 mm. The measured cross-sectional dimensions are listed in Table 2 and Table 3 for all the specimens belonging to geometry 1 and 2, respectively. It should be noted that the values reported in the tables are those obtained after accounting for the 0.04 mm nominal thickness of the zinc coating.

In order to assemble the specimens, holes with a nominal diameter of 6.25 mm were first drilled in one of the components at the appropriate locations, as indicated in Fig. 3. The components were then positioned in their built-up configuration and secured with clamps. Next, the first component (containing the holes) was used as a template to drill the holes in the adjacent components. This allowed for an easy assembly, avoiding any mismatch of the holes. Finally, the components were bolted together using grade 8.8 M6 bolts, and the clamps were removed. All bolts were tightened with a controlled torque of 10 Nm. This is representative of the torque exerted by a spanner when hand-tightening the bolts and did not introduce any significant pre-tensioning in the bolts. Fig. 4 shows the specimens after the assembly process.

3. Material Properties

A series of coupon tests was carried out in order to determine the material properties of the beams. The coupons were cut along the rolling direction of the material (i.e. the longitudinal direction of the beam) near the end section of one of the test specimens after testing. This location was chosen since the material had not been subjected to significant stress in this region during the test. For each type of channel component, two flat coupons were cut along the centre line of the web and two corner coupons were taken from the web-flange junction. The flat coupons had a nominal width of 12.5 mm, while the corner coupons had a nominal width of 6 mm. All coupons were instrumented with an extensometer of 50 mm gauge length. In addition, each flat coupon was instrumented with one 5 mm strain gauge on each side of the coupon, while each corner coupon was instrumented with a 5 mm strain gauge on the outside of the corner. Due to the asymmetric shape of the corner coupons they were tested in pairs with a square bar placed between the gripped ends of the coupons, as illustrated in Fig. 5.

The cross-sectional area of the curved corner coupon was determined by taking a macro photograph of the cross-section using the reversed lens technique. The images were then imported into AutoCAD® software (AutoCAD, 2014) and scaled based on the measurement of the width of the gripped end of the coupon, as illustrated in Fig. 6. The measured width of the coupon along the gauge length was then superimposed on the photograph, allowing the area to be automatically calculated by the software. The process was repeated with pictures taken from the other end of the coupon and a difference in the calculated areas of less than 1.5% was obtained for all coupons.

The tensile coupons were tested in a 300 kN Shimadzu AGS-X universal testing machine, while applying a displacement rate of 2 mm/min. Each test was halted for 2 minutes at regular intervals in order to allow the load to settle down to ‘static’ values and eliminate strain rate effects. The static stress-strain curves are shown in Fig. 7 for all coupons. Table 4 lists the (static) engineering values of the material properties obtained for each coupon, as well as average values for corresponding pairs. ($\sigma_{0.2\%}$) corresponds to the 0.2% proof stress, (σ_u) is the ultimate tensile strength and (ϵ_f) is the elongation after fracture measured over a gauge length of 50 mm.

4. Imperfection Measurements

The capacity and behaviour of thin-walled structural members in many cases exhibit pronounced sensitivity to geometric imperfections (Van der Neut, 1969; Becque, 2014). For this reason the imperfections of all specimens were recorded before testing using the measuring rig developed by Meza et. al (2018), which consisted of a nominally flat steel table and a traverse system powered by two electric motors (Fig. 8). The motors allowed the movement of a laser displacement sensor in two orthogonal directions along guiding bars. The imperfections in the guiding system were determined by taking readings of the nominally flat table in the absence of a test specimen and these imperfections were deducted from the

readings. Thus, an accuracy of approximately 0.06 mm was obtained, as this was the guaranteed flatness of the table. Readings were taken along different longitudinal lines on the specimen, as illustrated in Fig. 9, within the constant moment span. Whenever possible, the imperfections were recorded in the assembled state (as indicated by the red arrows in Fig. 9). However, the imperfections in the webs of the built-up specimens were recorded before assembling the top and bottom channels, as access was partially blocked in the assembled state (black arrows in Fig. 9).

The laser sensor was moved at a constant speed of 5 mm/s, while readings were taken with a sampling rate of 50 Hz, resulting in a reading every 0.1 mm.

The recorded imperfections were used to determine representative out-of-plane imperfections in the web (δ_{web}) and the flanges (δ_{flange}) of the channels. δ_{web} was determined as the out-of-plane imperfection recorded along the centre line of the web relative to the imperfections recorded along the corners. δ_{flange} was determined by first computing the out-of-plane imperfections along the flange tip relative to the imperfections recorded along the corner. However, since it was not possible to place the web of the channel in a vertical position with perfect accuracy during the readings, these initial values still contained an arbitrary constant offset, which was eliminated by expressing δ_{flange} relative to its average value along the beam. Fig. 10 shows typical imperfection profiles in a representative beam. The vertical dashed lines indicate the locations of the connectors. The complete imperfection data of all specimens can be found in Meza (2018). The maximum and the average values of δ_{web} and δ_{flange} are listed in Table 5 for the components of each geometry.

5. Connector behaviour

A series of single lap shear tests with two fasteners in the line of stress was carried out to determine the behaviour of the connectors used to assemble the built-up beams. The specimens were fabricated from steel strips taken from spare sections and a total of six tests

were carried out. The specimens labelled CB15-12 comprised ply thicknesses and connectors identical to the configuration encountered in the flanges of the built-up beams, while specimens CB15-15 were representative of the connectors located in the web. Three identical specimens were fabricated for each configuration in order to account for statistical variability in the results (i.e. six tests were carried out in total). Fig. 11 shows the test set-up. The dimensions of the test specimens were chosen following the recommendations given in ECCS TC7 (2009) and the specimens were assembled in the same way as the built-up beams. In particular, the same controlled torque of 10 Nm was used. All specimens were tested in a 300 kN Shimadzu universal testing machine and were loaded to failure at a displacement rate of 0.5 mm/min. Fig. 12 shows the typical recorded load-elongation behaviour. Further information about the connector tests, as well as complete results for all connector specimens, can be found in Meza (2018).

6. Test set-up

All 12 specimens were bent about their major axis using a four-point bending configuration, as illustrated in Fig. 13a. The test specimens were supported at their ends on rollers located 3000 mm apart. The actuator was connected to a spreader beam, which exerted concentrated loads onto the specimen through loading points which were implemented as simple supports (one roller and one pin) located 1600 mm apart. An adjustable lateral support system was used to restrain the spreader beam against any out-of-plane movement, as shown in Fig. 13b. Nylon blocks were used as bearing pads between the spreader beam and the uprights of the support system in order to reduce friction. The loading points under the spreader beam consisted of top and bottom assemblies (Fig. 14), which were bolted to the spreader beam and the test specimen, respectively, and contained vertical flanges to prevent out-of-plane displacements of the top flange of the test specimen.

The cross-sections of the test specimens above the supports were packed with wooden blocks which tightly fitted within the web and flanges. This eliminated possible bearing failure and also prevented a distortion of the cross-section characterized by a lateral displacement of the compression flange combined with bending of the web about a horizontal axis in its plane. This distortion originated from the tendency of the beam to fail in lateral-torsional buckling and this phenomenon was observed in beam B1-0a (which was tested without wooden blocks) after local buckling took place. This resulted in the beam being unable to reach the load attained by its twin specimen, and therefore the ultimate capacity obtained for specimen B1-0a was discarded.

Three LVDTs with a stroke of 50 mm were used to record the deflections of the beams under the loading points and at mid-span, as illustrated in Fig. 13a. Eight potentiometers with a stroke of 25 mm were also used to measure the buckling deformations of the components. These potentiometers were mounted on two identical yokes, which were attached to the bottom flange of the built-up cross-section, as shown in Fig. 15. As the test specimens underwent overall bending, the bottom flange of the built-up cross-section experienced tension and was not at risk of local buckling, while the yokes were able to move with the cross-section as a whole. Fig. 16 illustrates the positions of the yokes for each type of test specimen.

The specimens were tested in a reaction frame using an actuator with a capacity of 160 kN and a 50 kN load cell. The actuator was steered using a Cubus controller and a displacement rate of 1 mm/min was imposed. The tests were halted for 4 minutes slightly before the peak load was reached in order to allow the load to settle to its lower bound 'static' value. The specimens were deformed well beyond the peak load in order to identify the location where the plastic deformations localized. The data was also collected using the Cubus system, using a sampling rate of 1 Hz.

7. Test results

7.1 Geometry 1

All test specimens with geometry 1 failed within the constant moment span as a result of local buckling, with significant interaction taking place between the top channel and the channels comprising the web of the built-up cross-section. The top channel consistently buckled first, before buckling was observed in the channels comprising the webs. Fig. 17 illustrates the local buckling pattern, which typically contained 15 or 16 half-waves of fairly similar half-wavelength along the constant moment span. These buckles were estimated to have an average half-wavelength of around 100 mm. A slight exception occurred in beams B1-3, which displayed 17 half-waves, with two of the buckles being noticeably smaller than the others. This was attributed to the presence of the connectors. It is important to note that the observed half-wavelength of 100 mm was very close to the natural local buckle half-wavelength of 110 mm, calculated using CUFSM 4.05 (Schafer 2006) for the top channel in isolation. The web channels had a similar (calculated) natural local buckle half-wavelength of 100 mm, but the number of buckles generated in the web channels and the associated half-wavelength could not be experimentally determined as the magnitude of these buckles was not large enough to allow accurate measurements.

The potentiometers mounted on the yokes consistently revealed a locally buckled shape in the top channel which was symmetric about the plane of bending in the initial stages of buckling, with both lips buckling either inward or outward. The web channels, on the other hand, were recorded to buckle symmetrically with respect to the plane of bending only in those specimens without any connectors in the constant moment span (B1-0), while in the remaining specimens the buckling pattern was anti-symmetric. The symmetric buckling pattern of the web channels in the former specimens could be attributed to the fact that the channels were able to buckle largely independently from each other, without any connectors

in the constant moment span forcing them to remain in contact. In the specimens with 2 and 3 rows of connector, on the other hand, the connector spacings were short enough to force the web channels to buckle in a synchronous manner. This is illustrated in Fig. 18, which shows the out-of-plane displacements of the components of beam B1-3a against the applied load. The solid and dashed lines in this figure represent the readings obtained from the set of potentiometers placed on each of the two yokes. Positive values indicate displacements towards the potentiometer (outward displacements of the channel) while negative values indicate displacements away from the potentiometers (inward displacements of the channel). In the specimens with two or three sets of intermediate connectors along the constant moment span, the buckling pattern of the top channel was affected by subsequent buckling of the web channels, as illustrated by Fig. 18. In order to accommodate the buckling pattern of the web channels a modification of the buckle half-wavelength occurred in the top channel. This is reflected in a rather sudden change of the amplitude of the buckles of the top channel recorded locally by the potentiometers (followed in some cases by a reversal in direction). The closer the connector spacing, the more pronounced this effect was.

Despite the similarity of the initial buckling pattern observed in each pair of twin specimens, upon reaching the peak load the plastic deformations generally localized in different locations. Yield lines simultaneously developed in the top channel and in the web and the top flange of the channels comprising the web of the built-up specimens, resulting in a hinge-like behaviour. In general, the yield line pattern in the top channel was symmetric with respect to the plane of bending, while that in the web channels was anti-symmetric, as shown in Fig. 19. An exception to this occurred in specimens B1-0b and B1-2b, in which the top channel developed an asymmetric yield line pattern near mid-span. This was accompanied by the top flange undergoing limited out-of-plane displacements, combined with twisting of the cross-section along the constant moment span, while a second ‘hinge’ appeared near one of the

loading points, as shown in Fig. 20. However, these out-of-plane displacements did not occur until after the peak load was reached and therefore all beams could be considered fully laterally restrained until the test specimens had reached their ultimate capacity.

7.2 Geometry 2

In general, the specimens with geometry 2 failed within the constant moment span by local buckling. Fig. 21 illustrates the typical local buckling pattern. However, in the beams without intermediate connectors (B2-0), flexural-torsional buckling of the top channel as an individual component was observed to interact with local buckling near the peak load. In the case of beam B2-0a this occurred shortly after the local buckling deformations in the top channel localized near mid-span, resulting in localized twisting, as illustrated in Fig. 22. However, in specimen B2-0b the interaction between local buckling and flexural-torsional buckling of the top channel was more significant, causing the top channel to twist with a half-wavelength of approximately 750 mm before the specimen reached its ultimate capacity, as shown in Fig. 23.

In all test specimens the top channel buckled locally before the web channels and the amplitude of its buckles was significantly larger. The top channel displayed between 14 and 16 half-waves along the constant moment span with fairly similar half-wavelength. Although the number of half-waves generated in the web channels was not easily discerned due to their small amplitude, it was noted that in specimens B2-2 one of the buckles had a half-wavelength significantly larger than the others. Despite the difficulty in distinguishing the half-waves in the web channels it was estimated to also be between 14 and 16 within the constant moment span. This resulted in half-wavelengths in the top channel and the web channels ranging from approximately 94 mm to 107 mm. These values were very close to the natural local buckling half-wavelengths calculated using CUFSM 4.05 (Schafer 2006) for the

top channel and the web channels in isolation, which were 120 mm and 100 mm, respectively.

In the beams without intermediate connectors (B2-0), a gap developed along the constant moment span between the top channel and the web channels while the specimens deformed. This gap was more pronounced around mid-span, allowing a larger amplitude of the buckles in the top flange of the web channels to develop in this region. On the other hand, towards the ends of the constant moment span, where the components were in closer contact with each other, the amplitude of the buckles in the top flange of the web channels was considerably smaller, to the point that it was difficult to observe them.

In beams B2-2, the top channel also tended to separate from the web channels, especially at mid-span. However, the intermediate connectors opposed this separation, thereby pulling the flanges of the web channel upward, as illustrated in Fig. 24.

In beams B2-3, no gap originated. In these specimens the top channels displayed exactly four buckled half-waves between connectors, resulting in 16 half-waves along the constant moment span.

The potentiometers consistently recorded a buckling pattern in the top channels which was initially symmetric with respect to the plane of bending, while the web channels were recorded to buckle in an anti-symmetric shape. As a typical example, Fig. 25 shows the measured out-of-plane deformations of the components of beam B2-3a. The potentiometers mounted on the yoke located to the left (solid black lines) and to the right (dashed black lines) of mid-span recorded both flanges of the top channel to buckle inward. In the yoke located to the right of mid-span one of the potentiometers recorded an inward deformation in the web, while the other potentiometer recorded an outward deformation (as shown by the red lines).

In general, the readings from the potentiometers did not show the buckling pattern of the top channels to be affected by subsequent buckling of the web channels to the same degree as in the specimens with geometry 1. A noticeable interaction between the components leading to a definite change in the locally recorded amplitude of the buckles in the top channel was only observed in beam B2-3b.

Although the buckling pattern observed in twin specimens was generally similar until the ultimate capacity was reached, localization of the buckling pattern often occurred at different locations along the constant moment region. As the built-up specimens deformed beyond their ultimate capacity, yield lines appeared in the top channel and in the top flange of the web channels. As this mechanism developed further, the built-up cross-sections generally experienced some twisting and lateral displacement in the neighbourhood of the resulting 'hinge'. These deformations gradually spread over the whole constant moment span as the specimen continued to deflect. However, this phenomenon only occurred during the descending part of the load-deflection curve and the beams could be considered to be sufficiently laterally restrained until they reached their ultimate capacity. Fig. 26 shows the yield line mechanism which developed in a typical specimen.

7.3 Critical buckling stresses

The buckling stresses of the individual cross-sectional components were determined from the readings of the potentiometers, using the prediction of classical perturbation theory that the initial post-buckling deformations, when plotted against the load, follow a parabolic shape (Venkataramaiah and Roorda, 1982). This is illustrated in Fig. 27. Since the top channel was the first component to buckle in all of the test specimens, its critical buckling stress could be estimated from the recorded bending moment, assuming that no slip occurred in the connections prior to buckling, so that plane sections remained plane:

$$\sigma_{cr} = \frac{M_{cr} y_{max}}{I_{xx}} \quad (1)$$

where I_{xx} is the second moment of area of the built-up cross-section about the horizontal axis through its centroid, y_{max} is the distance from the centroid of the built-up section to the extreme compression fibre and M_{cr} is the moment at which the potentiometers indicated buckling to occur. The stress given by Eq. (1) provides an upper bound to the actual critical stress because the finite shear stiffness of the connections is not accounted for. After buckling of the top channels occurred the stress distribution in these channels was expected to become highly non-linear, so that the critical buckling stress of the web channels could no longer be determined using an analogous procedure.

For each beam the experimentally derived buckling stress of the top channel was compared to the theoretical buckling stress obtained from an elastic stability analysis carried out using CUFSM 4.05 (Schafer, 2006). In this analysis the buckling stresses were determined based on the average measured cross-sectional dimensions and the Young's modulus obtained from the flat tensile coupons. The top channel was considered in isolation, without any interaction with the rest of the cross-section, but under a stress gradient consistent with the plane section assumption and using the buckle half-wavelength observed during the test.

In order to confirm that no slip occurred in the connections between the top channel and the web channels prior to buckling, the shear force in the connectors located along the shear span was calculated using Zhuravsky's equation (Timoshenko, 1940):

$$V_{con} = \frac{V \cdot A_{top} \cdot \bar{y}}{16 I_{xx}} L_s \quad (2)$$

In the above equation V_{con} is the shear force in the connector, V is the shear force in the beam, A_{top} is the cross-sectional area of the top channel, \bar{y} is the distance from the centroid of the top channel to the centroid of the built-up cross-section, as illustrated in Fig. 28 for both geometries, and L_s is the length of the shear span. The resulting shear force is compared to

the slip force of the connectors, obtained from Section 5, in Table 6. The comparison indicates that no slip occurred in the connections prior to buckling of the top channels. Consequently, the plane section assumption used in the calculation of both the theoretical and the experimental buckling stress of the top channel was valid in good approximation.

Table 7 compares the theoretical critical buckling stresses of the top channels with the experimentally derived values. For some of the test specimens the potentiometers located on the two different yokes captured the onset of local buckling in the top channel at slightly different stress levels, in which case both readings were included in Table 7. In the beams with geometry 1 the experimental buckling stresses were, on average, 40 % higher than the theoretical buckling stresses of the isolated channel. This demonstrated that the top channel benefited significantly from the restraint provided by the unbuckled web channels. In the beams with geometry 2, on the other hand, the experimentally derived buckling stresses generally coincided well with the theoretical ones, indicating that the top channel in these specimens did not noticeably benefit from any restraint provided by the unbuckled web channels.

While no slip occurred in the connectors before buckling of the top channel took place in any of the specimens, once the specimens deformed beyond their ultimate capacity some relative movement between the components was generally noticed in the end sections of the built-up beams. This slip measured between 1 and 2 mm at the end of the test.

7.4 Ultimate capacity

Figs. 29 and 30 plot the bending moment against the relative deflection at mid-span for all specimens with built-up geometry 1 and 2, respectively. The mid-span deflection was thereby considered relative to the deflections of the beam under the loading points. ‘Static’ moments were plotted, which were obtained after accounting for the decrease in moment observed

when halting the test for 4 minutes shortly before the peak load in order to eliminate strain rate dependent effects.

The ultimate moment capacities obtained for all beams, as well as the average values of the ultimate capacity for each set of twin specimens, are listed in Table 8. Good agreement in the ultimate capacity was generally achieved within each pair of twin specimens. As previously discussed, beam B1-0a failed prematurely as a result of being tested without wooden blocking over the supports, causing the end sections to distort, accompanied by in-plane bending of the top flange. Consequently, the ultimate capacity recorded for test B1-0a was discarded. The twin specimens of beams B1-2 and B1-3 showed small differences in the ultimate capacity of 6 % and 2 %, respectively.

Regarding the specimens with geometry 2, the B2-0 specimens showed the maximum difference in ultimate capacity, which amounted to 11 %. This can be attributed to the fact that in these specimens flexural-torsional buckling of the top channel was observed to interact with local buckling. The interaction of global and local modes is notoriously imperfection sensitive, which might explain why the flexural-torsional mode appeared slightly earlier over the loading history in specimen B2-0b and the interaction was somewhat more pronounced, resulting in a lower ultimate capacity. In beams B2-2 and B2-3, on the other hand, the difference in ultimate capacity between twin specimens was 2 % and 1 %, respectively.

The test results showed that reducing the connector spacing in the constant moment span resulted in a modest increase in the ultimate capacity of the specimens with geometry 1. The beams with two rows of intermediate connectors experienced an average increase in the ultimate capacity of 3 % relative to the beam without connectors, while the specimens with three rows of connectors exhibited an average increase of 11 %.

The specimens with geometry 2 showed a more substantial increase in ultimate capacity when the spacing between the connectors was reduced. The beams with two intermediate

rows of connectors along the constant moment span experienced an average increase in ultimate capacity of 22 % relative to the beams without intermediate connectors, while the beams with three rows of intermediate connectors displayed an average increase of 36 %. This can in part be attributed to the elimination of the flexural-torsional mode for shorter connector spacings.

Conclusions

An experimental program investigating CFS built-up beams, encompassing 12 specimens with two different cross-sectional geometries, is presented in this paper. The built-up specimens were composed of plain channel components assembled using M6 bolts, while varying the connector spacing among specimens. All beams were tested in a four-point bending configuration and lateral restraints were provided at the loading points in order to avoid global instability of the built-up specimen. The geometric imperfections of the test specimens were measured using a laser sensor prior to testing, while the material properties of the constituent channels were determined by testing a series of tensile coupons.

The specimens with geometry 1 all failed by local buckling, with the top channel consistently being the first component to buckle. The observed buckle half-wavelengths were close to the natural half-wavelengths of the isolated components, regardless of the connector spacing. However, a comparison of the experimentally derived critical buckling stresses of the top channel with the theoretical buckling stress of the channel in isolation revealed that the top channel benefitted significantly from the restraint provided by the web channels.

The specimens with geometry 2 failed by local buckling, while flexural-torsional buckling of the top channel in between connector points was also observed in the specimens with the largest connector spacing. The experimentally measured buckle half-wavelengths and critical buckling stresses of the top channel agreed well with those calculated for the isolated channel, indicating a minimal amount of restraint exerted by the web channels onto the top

channel. A tendency of the top channel to separate from the web channels was also observed, which was counteracted by the connectors.

In both geometries it was observed that the components of the cross-section were forced to adjust their buckling patterns relative to their preferred patterns as isolated components, as a result of the connections and the contact between components. This manifested itself in a reduction of the amplitude of the buckles or a constraint on the direction of the buckling displacements due to contact between the components, and a minor adjustment of the half-wavelength of the buckles due to the constraints provided by the connectors.

The specimens with geometry 1 showed a relatively modest increase in the ultimate capacity when reducing the connector spacing, while the ultimate capacity of the specimens with geometry 2 was more significantly affected by the connector spacing. More specifically, reducing the connector spacing from 1500 mm to 375 mm resulted in increases in the ultimate capacity of 11 % and 36 % for the specimens with geometry 1 and 2, respectively.

The presented research is part of a wider investigation into built-up cold-formed structural members (Meza et al. 2016, Meza 2018, Meza et al. 2019). The data gathered from the experiments will be used to develop accurate FE models which will serve as a tool to further study the the behaviour of built-up CFS members through parametric studies. The eventual goal is to develop accurate, safe and reliable design guidelines for these types of structural members for the benefit of practitioners.

Data availability statement

Some or all data, models, or code generated or used during the study are available from the corresponding author by request. Material properties data, geometric imperfections data, connector behavior data, and out-of-plane deformation data.

Acknowledgement

The authors are grateful for the financial support provided by the EPSRC through grant EP/M011976/1.

References

- AISI (American Iron and Steel Institute). (2016). "North American Specification for the Design of Cold-Formed Steel Structural Members." AISI S136-16, Toronto, ON.
- AutoCAD (2014). AutoCad software, Autodesk Inc., San Rafael, CA, USA
- Becque, J. (2014), "Local-overall interaction buckling of inelastic columns: A numerical study of the inelastic Van der Neut column", *Thin-Walled Structures*. 81, 101–107.
- Blum, H.B. and Rasmussen, K.J.R. (2019). "Experimental Investigation of Long-Span Cold-Formed Steel Double Channel Portal Frames." *Journal of Constructional Steel Research*. 155, 316–330.
- CEN (European Committee for Standardization). (2004). "Continuously hot-dip coated strip and sheet of structural steels – Technical delivery conditions, EN 10326, Brussels.
- CEN (European Committee for Standardization). (2005). "Design of steel structures, Part 1.1: General rules and rules for buildings, EN 1993-1-1, Brussels.
- CEN (European Committee for Standardization). (2016). "Designation systems for steels, Part 1: Steel names, EN 10024-1, Brussels.
- Dang, K. P. and Rasmussen, K.J.R. (2018). "Flexural rigidity of cold-formed steel built-up members." *Thin-Walled Structures*. 140, 438–449.
- Di Lorenzo, G., Portioli, F. and Landolfo, R. (2004). "On the Characterization of the Material Properties for Cold-Formed Steel Members." *Proc., Fourth International Conference On Thin-Walled Structures*, pp. 251–258.
- Di Lorenzo, G., Portioli, F. and Landolfo, R. (2006). "Experimental Investigation on the Load Bearing Capacity of Built-up Cold-Formed Steel Beams." *Proceedings of International Colloquium on Stability and Ductility of Steel Structures, Lisbon*.
- Dubina, D., Stratan, A. and Nagy, Z. (2009). "Full - scale tests on cold-formed steel pitched-roof portal frames with bolted joints." *Advanced Steel Construction*, 5, 175–194.
- ECCS TC7 (2009), *The Testing of Connections with Mechanical Fasteners in Steel Sheeting and Sections*.
- Fratamico, D.C., Torabian, S., Zhao, X., Rasmussen, K.J.R. and Schafer, B.W. (2018). "Experiments on the global buckling and collapse of built-up cold-formed steel columns." *Journal of Constructional Steel Research*, 144, 65–80.
- Jeyaragan, S. and Mahendran, M. (2008a). "Experimental Investigation of the New Built-up LiteSteel Beams." *Proc., Fifth International Conference on Thin-Walled Structures, Brisbane, Australia*.
- Jeyaragan, S. and Mahendran, M. (2008b). "Numerical Modelling and Design of the New Built-up LiteSteel Beams." *Proc., Fifth International Conference on Coupled Instabilities in Metal Structures, Sydney, Australia*.

- Landolfo, R., Mammana, O., Portioli, F., Di Lorenzo, G. and Guerrieri, M.R. (2008). "Laser welded built-up cold-formed steel beams: Experimental investigations." *Thin-Walled Structures*, 46, 781–791.
- Landolfo, R., Mammana, O., Portioli, F., Di Lorenzo, G. and Guerrieri, M.R. (2009). "Experimental investigation on laser welded connections for built-up cold-formed steel beams." *Journal of Constructional Steel Research*, 65, 196–208.
- Lim, J.B.P. and Nethercot, D.A. (2002). "Design and Development of a General Cold-Formed Steel Portal Framing System." *Structural Engineer*. 80, 31–39.
- Meza, F. J. (2018). "The Behaviour of Cold-Formed Steel Built-up Structural Members." PhD thesis, The University of Sheffield, UK.
- Meza, F. J., Becque, J. and Hajirasouliha, I. (2019). "Experimental Study of Cold-Formed Steel Built-up Columns." *Thin-Walled Structures*, In press.
- Meza, F., Cheng, S., Becque, J., and Hajirasouliha, I. (2016). "Experimental investigation of the cross-sectional stability of cold-formed steel built-up columns." *Proceedings of the International Colloquium on Stability and Ductility of Steel Structures SDSS2016*, Timisoara, Romania.
- Portioli, F., Di Lorenzo, G. Landolfo, R. and Mazzolani, F.M. (2012). "Contact Buckling Effects in Built-up Cold-Formed Steel Beams." *Proc., The 6th International Conference on Coupled Instabilities in Metal Structures*, pp. 1–8.
- Schafer, B.W. (2006). "Buckling analysis of cold-formed steel members using CUFSM: conventional and constrained finite strip methods." *Proc., 18th International Specialty Conference on Cold-Formed Steel Structures*, Orlando, Florida.
- Timoshenko, S. (1940), *Strength of Materials-Part 1: Elementary Theory and Problems*, Second edition, D. Van Nostrand Company, Inc, New York.
- Van der Neut, A. (1969), "The interaction of local buckling and column failure of thin-walled compression members", *Proceedings 12th International Congress of Applied Mechanics*. pp. 389–399.
- Venkataramaiah, K.R. and Roorda, J. (1982). "Analysis of Local Plate Buckling Experimental Data." *Proc., Sixth International Specialty Conference on Cold-Formed Steel Structures*, St. Louis, Missouri, pp. 45–73.
- Wang, L. and Young, B. (2015). "Beam tests of cold-formed steel built-up sections with web perforations." *Journal of Constructional Steel Research*, 115, 18–33.
- Wang, L. and Young, B. (2016a). "Behavior of Cold-Formed Steel Built-Up Sections with Intermediate Stiffeners under Bending. I: Tests and Numerical Validation." *Journal of Structural Engineering*, 142.
- Wang, L. and Young, B. (2016b). "Behavior of Cold-Formed Steel Built-Up Sections with Intermediate Stiffeners under Bending. II: Parametric Study and Design." *Journal of Structural Engineering*, 142.
- Zhang, X. and Rasmussen, K. (2014). "Tests of cold-formed steel portal frames with slender sections." *Steel Construction*, 7, 199–203.

Table 1. Nominal dimensions of the component sections

| Beam | Section | h (mm) | b (mm) | t (mm) | r_{int} (mm) |
|------|---------|-------------|-------------|-------------|-------------------|
| B1 | T12915 | 129 | 48 | 1.5 | 3.0 |
| | T10412 | 104 | 42 | 1.2 | 2.4 |
| B2 | T12915 | 129 | 48 | 1.5 | 3.0 |
| | T10412 | 104 | 42 | 1.2 | 2.4 |

Table 2. Measured dimensions of specimens with geometry 1

| Beam | Web channels | | | | Flange channels | | | |
|----------|--------------|-------------|----------------|-------------------|-----------------|-------------|----------------|-------------------|
| | section | Web (mm) | Flange (mm) | Thickness (mm) | section | Web (mm) | Flange (mm) | Thickness (mm) |
| B1-0a | T12915-1 | 129.36 | 43.38 | 1.493 | T10412-1 | 104.35 | 39.82 | 1.141 |
| | T12915-2 | 129.15 | 43.49 | 1.487 | T10412-2 | 104.10 | 39.92 | 1.139 |
| B1-0b | T12915-3 | 129.31 | 43.48 | 1.495 | T10412-3 | 104.24 | 39.95 | 1.136 |
| | T12915-4 | 129.20 | 43.45 | 1.493 | T10412-4 | 104.05 | 39.72 | 1.137 |
| B1-2a | T12915-5 | 129.26 | 43.45 | 1.489 | T10412-5 | 103.95 | 39.94 | 1.137 |
| | T12915-6 | 129.13 | 43.53 | 1.496 | T10412-6 | 104.06 | 40.04 | 1.139 |
| B1-2b | T12915-7 | 128.95 | 43.78 | 1.501 | T10412-7 | 104.04 | 39.99 | 1.139 |
| | T12915-8 | 129.02 | 43.66 | 1.496 | T10412-8 | 104.01 | 39.97 | 1.144 |
| B1-3a | T12915-9 | 128.93 | 43.74 | 1.498 | T10412-9 | 103.95 | 39.98 | 1.141 |
| | T12915-10 | 128.90 | 43.69 | 1.501 | T10412-10 | 104.18 | 39.97 | 1.140 |
| B1-3b | T12915-11 | 128.83 | 43.70 | 1.506 | T10412-11 | 104.22 | 39.86 | 1.147 |
| | T12915-12 | 128.87 | 43.69 | 1.497 | T10412-12 | 103.96 | 39.93 | 1.146 |
| Average | | 129.08 | 43.59 | 1.496 | | 104.09 | 39.92 | 1.141 |
| St. Dev. | | 0.183 | 0.136 | 0.005 | | 0.129 | 0.087 | 0.004 |

Table 3. Measured dimensions of specimens with geometry 2

| Beam | Web channels | | | | Flange channels | | | |
|----------|--------------|-------------|----------------|-------------------|-----------------|-------------|----------------|-------------------|
| | section | Web (mm) | Flange (mm) | Thickness (mm) | section | Web (mm) | Flange (mm) | Thickness (mm) |
| B2-0a | T12915-1 | 129.28 | 43.42 | 1.486 | T10412-1 | 104.11 | 39.71 | 1.141 |
| | T12915-2 | 129.25 | 43.45 | 1.487 | - | | | |
| B2-0b | T12915-3 | 129.41 | 43.40 | 1.489 | T10412-2 | 104.04 | 39.92 | 1.136 |
| | T12915-4 | 129.13 | 43.44 | 1.490 | - | | | |
| B2-2a | T12915-5 | 129.05 | 43.65 | 1.495 | T10412-3 | 103.99 | 39.71 | 1.137 |
| | T12915-6 | 129.14 | 43.49 | 1.494 | - | | | |
| B2-2b | T12915-7 | 128.80 | 43.69 | 1.495 | T10412-4 | 103.89 | 39.76 | 1.137 |
| | T12915-8 | 128.84 | 43.72 | 1.495 | - | | | |
| B2-3a | T12915-9 | 129.02 | 43.69 | 1.507 | T10412-5 | 103.98 | 39.78 | 1.133 |
| | T12915-10 | 128.85 | 43.62 | 1.504 | - | | | |
| B2-3b | T12915-11 | 128.91 | 43.63 | 1.506 | T10412-6 | 103.95 | 39.70 | 1.134 |
| | T12915-12 | 129.07 | 43.61 | 1.508 | - | | | |
| Average | | 129.06 | 43.57 | 1.496 | | 103.99 | 39.76 | 1.136 |
| St. Dev. | | 0.201 | 0.123 | 0.007 | | 0.076 | 0.083 | 0.003 |

Table 4. Material properties of tensile coupons

| Type | Section | E (GPa) | | $\sigma_{0.2\%}$ (MPa) | | σ_u (MPa) | | ε_f (%) | |
|--------|----------|--------------|------|---------------------------|------|---------------------|------|------------------------|------|
| | | Ind. | Avg. | Ind. | Avg. | Ind. | Avg. | Ind. | Avg. |
| Flat | T10412-a | 212 | 208 | 432 | 426 | 471 | 466 | 14 | 14 |
| Flat | T10412-b | 204 | | 419 | | 461 | | | |
| Flat | T12915-a | 201 | 204 | 544 | 531 | 628 | 619 | 13 | 13 |
| Flat | T12915-b | 207 | | 518 | | 610 | | | |
| Corner | T10412-a | 193 | 198 | - | 460 | - | 479 | - | 3 |
| Corner | T10412-b | 202 | | - | | - | | | |
| Corner | T12915-a | 211 | 218 | - | 585 | - | 645 | - | 5 |
| Corner | T12915-b | 225 | | - | | - | | | |

Table 5. Maximum and average imperfections

| Specimen | Section | Imperfection (mm) | | |
|----------|---------|-------------------|------|------|
| | | | Max. | Avg. |
| B1 | T12915 | δ_{web} | 0.24 | 0.07 |
| | T10412 | δ_{web} | 0.25 | 0.07 |
| | | δ_{flange} | 0.49 | 0.00 |
| B2 | T12915 | δ_{web} | 0.24 | 0.07 |
| | T10412 | δ_{web} | 0.35 | 0.11 |
| | | δ_{flange} | 0.51 | 0.00 |

Table 6. Shear force in shear span connectors

| Specimen | V_{con} (N) | V_{slip} (N) | V_{slip}/V_{con} (-) |
|----------|------------------|-------------------|---------------------------|
| B1-0a | 1528 | 2600 | 1.702 |
| B1-0b | 1881 | 2600 | 1.382 |
| B1-2a | 2010 | 2600 | 1.294 |
| B1-2b | 1836 | 2600 | 1.416 |
| B1-3a | 1573 | 2600 | 1.653 |
| B1-3b | 1490 | 2600 | 1.745 |
| B2-0a | 1044 | 2600 | 2.490 |
| B2-0b | 954 | 2600 | 2.725 |
| B2-2a | 1091 | 2600 | 2.383 |
| B2-2b | 1041 | 2600 | 2.498 |

| | | | |
|-------|------|------|-------|
| B2-3a | 1087 | 2600 | 2.392 |
| B2-3b | 1035 | 2600 | 2.512 |

Table 7. Buckling stresses of the top channel

| Specimen | Component section | Theoretical buckling stress (MPa) | Buckling stress from test (MPa) | Buckling stress from test /Theoretical buckling stress |
|----------|-------------------|-----------------------------------|---------------------------------|--|
| B1-0a | T10412-1 | 107 | 138 | 1.29 |
| B1-0b | T10412-3 | 111 | 170 | 1.53 |
| B1-2a | T10412-5 | 106 | 170 | 1.60 |
| B1-2b | T10412-7 | 109 | 154-166 | 1.41-1.52 |
| B1-3a | T10412-9 | 107 | 142 | 1.33 |
| B1-3b | T10412-11 | 108 | 126-134 | 1.17-1.24 |
| B2-0a | T10412-1 | 126 | 127 | 1.01 |
| B2-0b | T10412-2 | 126 | 120-142 | 0.95-1.13 |
| B2-2a | T10412-3 | 127 | 133-152 | 1.05-1.20 |
| B2-2b | T10412-4 | 127 | 121-136 | 0.95-1.07 |
| B2-3a | T10412-5 | 128 | 133 | 1.04 |
| B2-3b | T10412-6 | 128 | 128 | 1.00 |

Table 8. Ultimate capacities

| Beam | Ultimate Moment (kNm) | Average Ultimate Moment (kNm) |
|-------|-----------------------|-------------------------------|
| B1-0a | - | 11.84 |
| B1-0b | 11.84 | |
| B1-2a | 12.51 | 12.17 |
| B1-2b | 11.83 | |
| B1-3a | 13.28 | 13.14 |
| B1-3b | 13.01 | |
| B2-0a | 9.08 | 8.63 |
| B2-0b | 8.19 | |
| B2-2a | 10.41 | 10.53 |
| B2-2b | 10.64 | |
| B2-3a | 11.66 | 11.70 |
| B2-3b | 11.74 | |

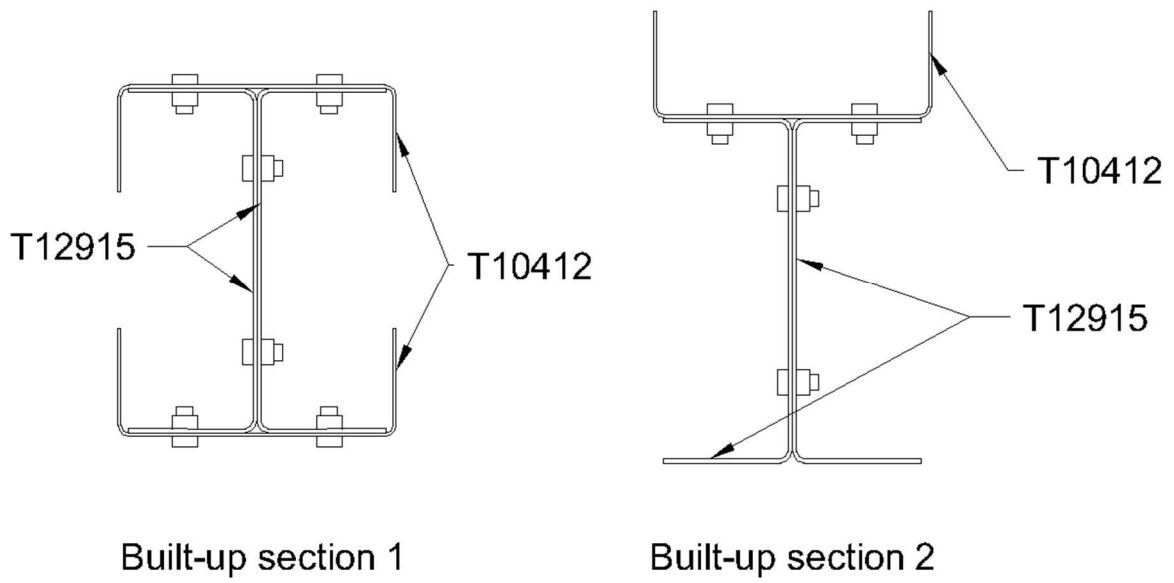


Fig. 1. Cross-sectional geometries

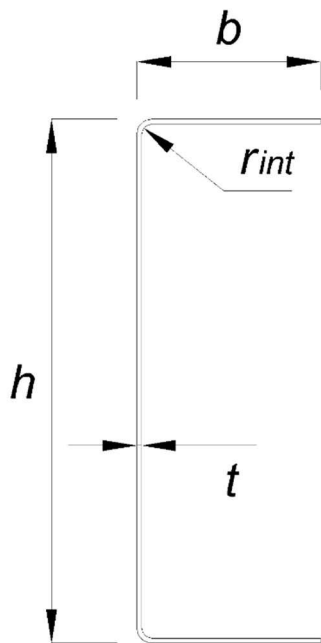


Fig. 2. Nomenclature used to refer to the dimensions of the component sections

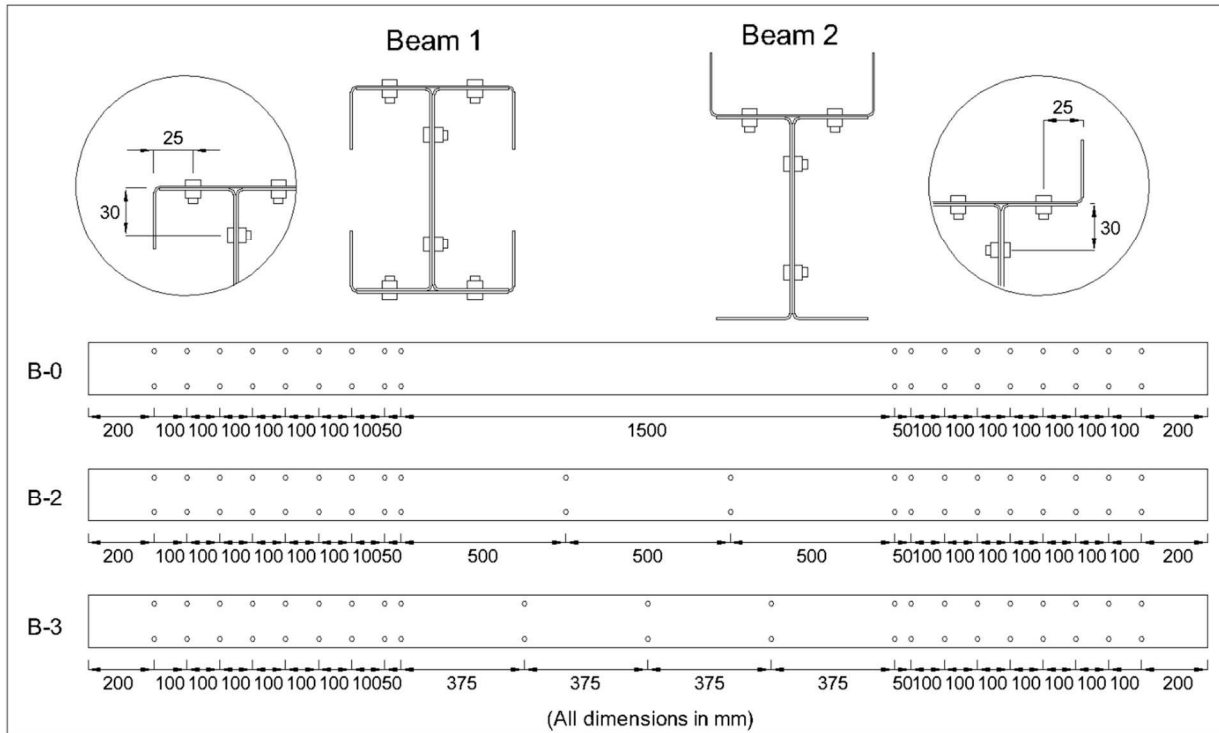


Fig. 3. Location of connectors in beams with geometries 1 and 2

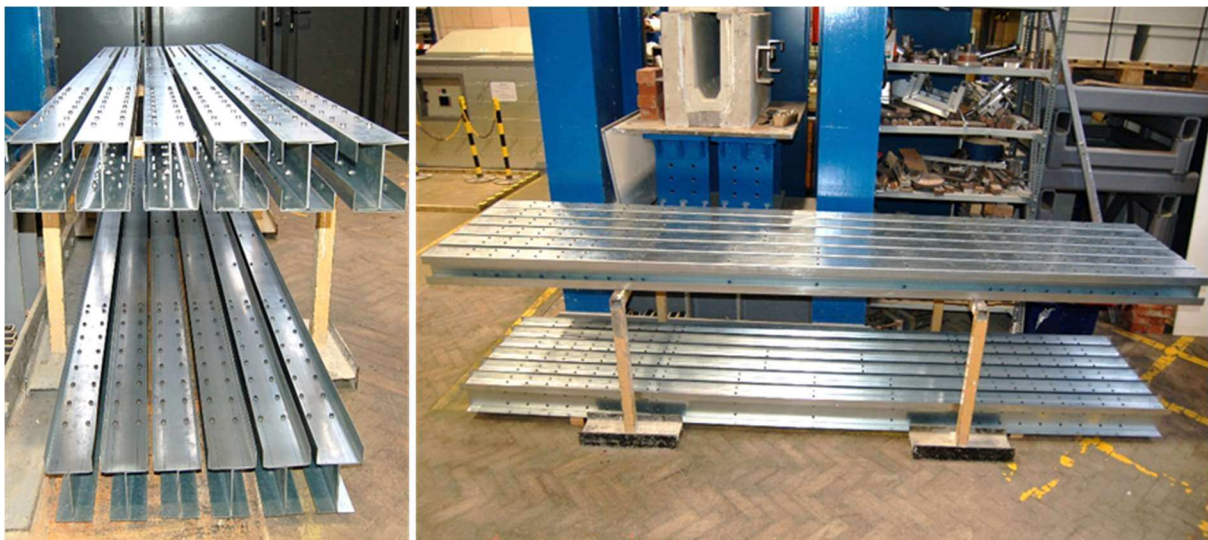


Fig. 4. Built-up beams after assembly

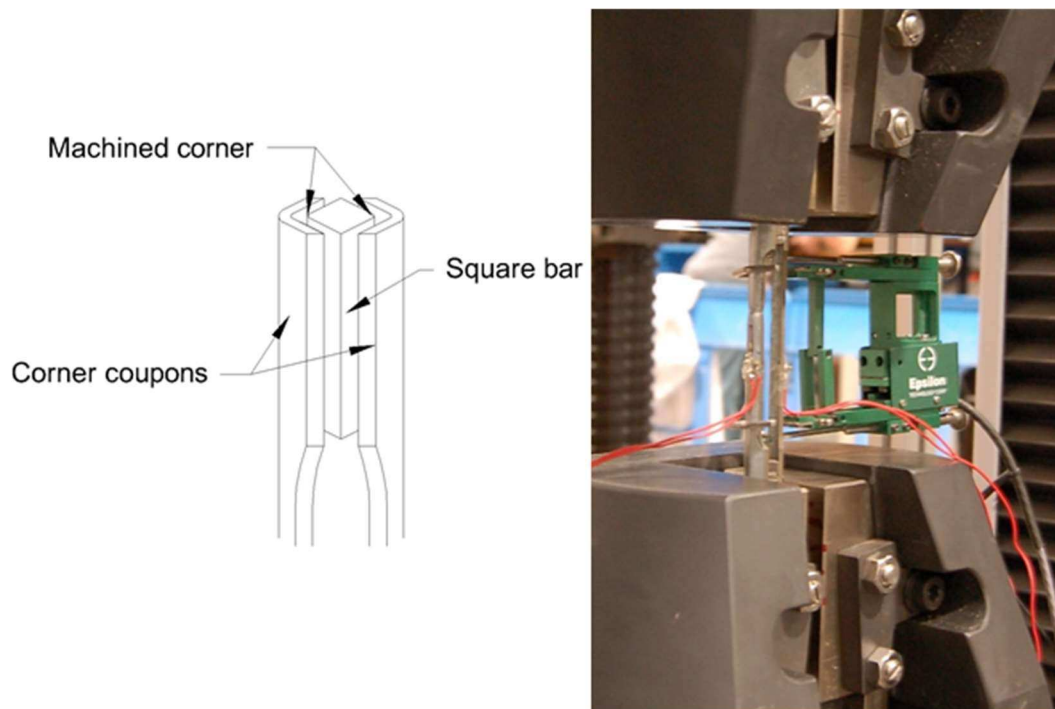


Fig. 5. Corner coupon test set-up

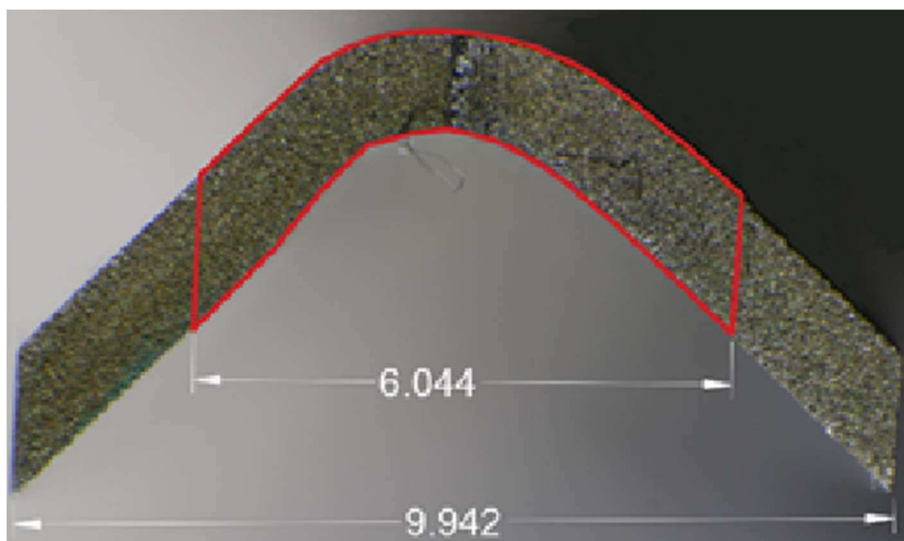


Fig. 6. Macro photograph of the cross-section of a corner coupon

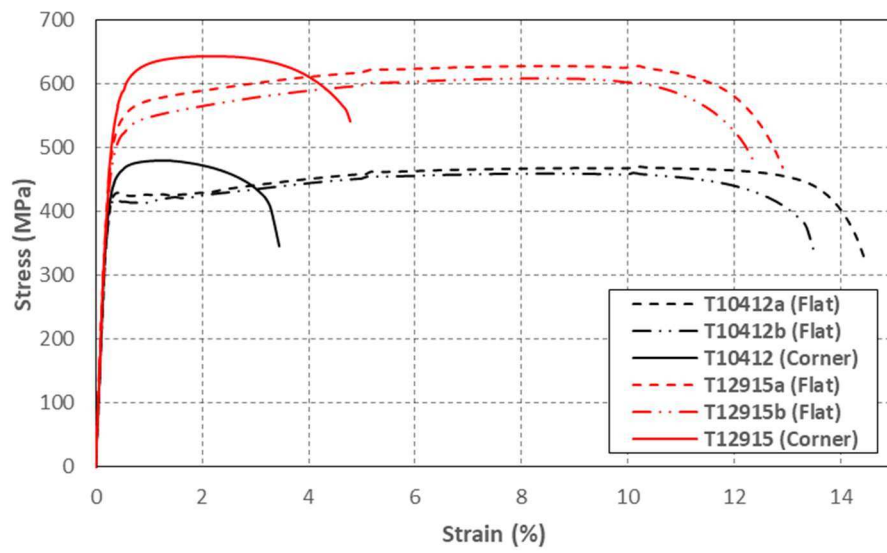


Fig. 7. Stress-strain curves of flat and corner coupons

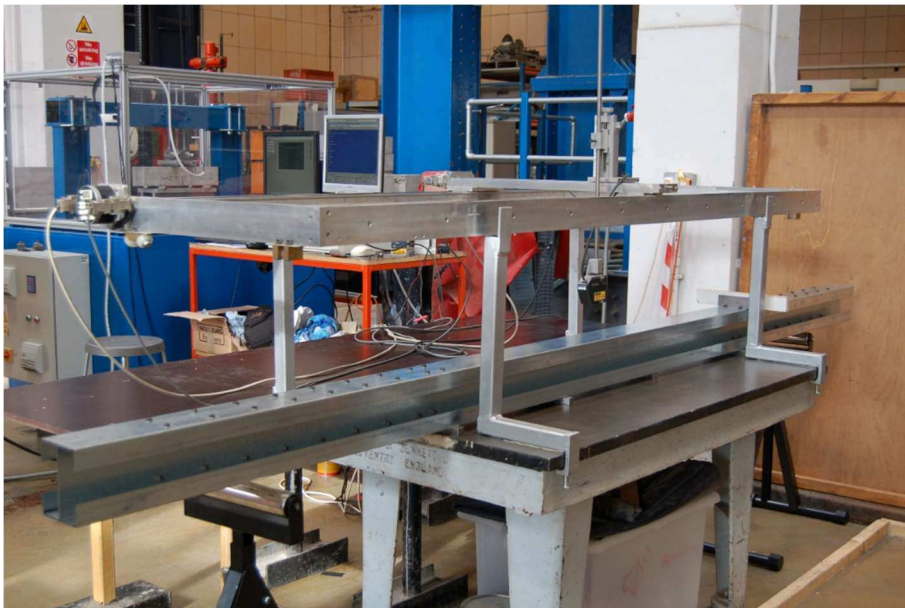


Fig. 8. Imperfection measurement rig

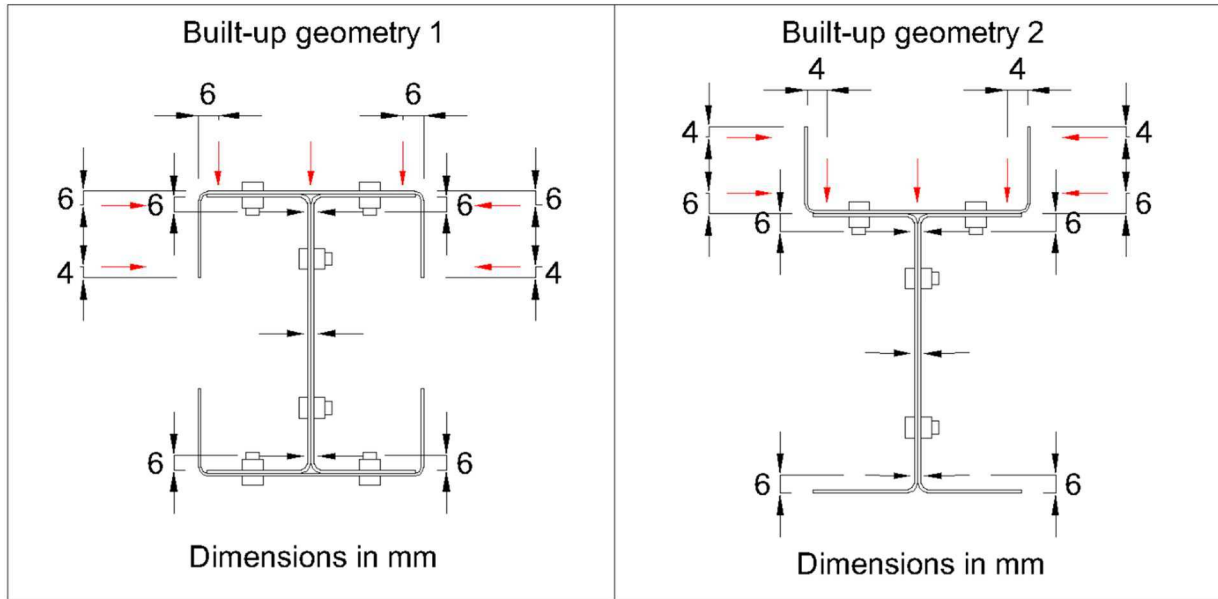


Fig. 9. Locations of the imperfection measurements

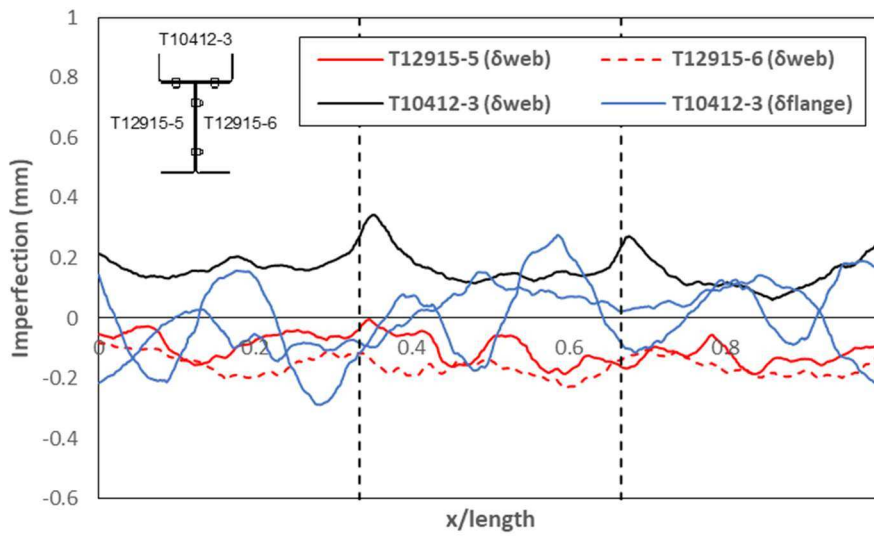


Fig. 10. Out-of-plane imperfections of beam B2-2a

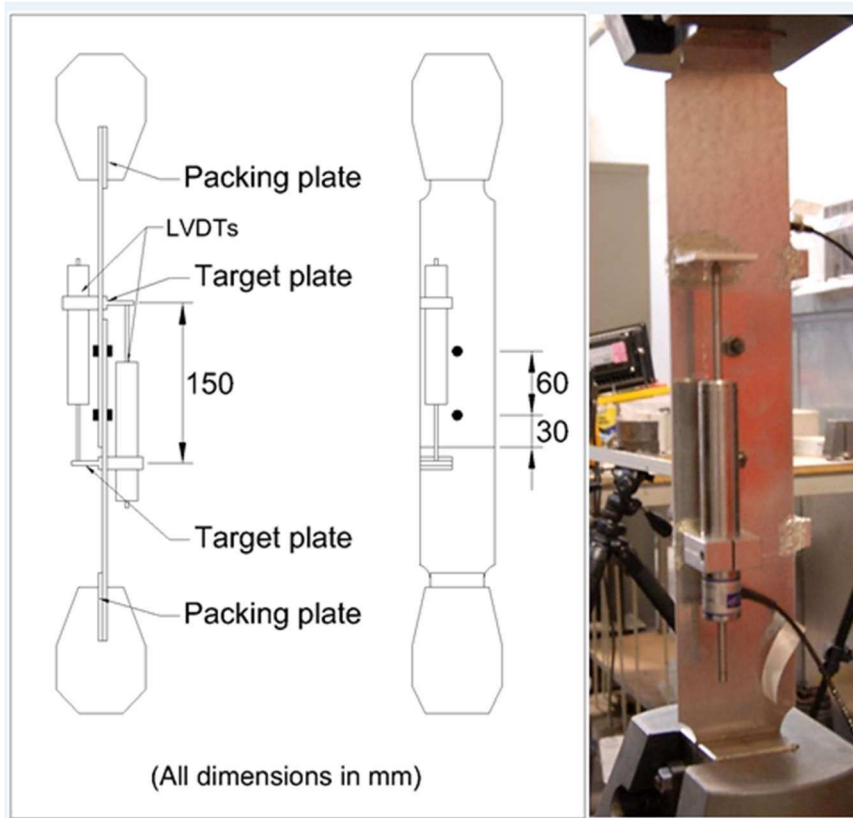


Fig. 11. Single lap shear test set-up

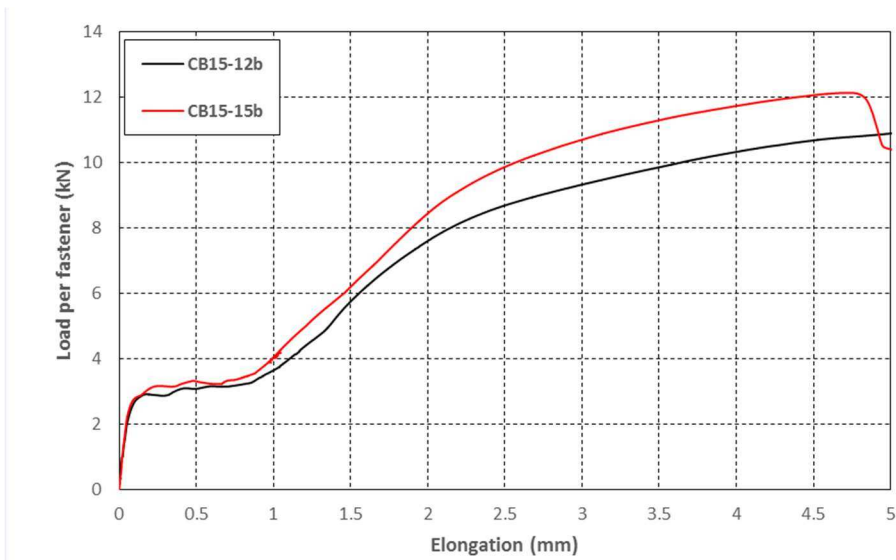


Fig. 12. Load-elongation behaviour of connector test specimens

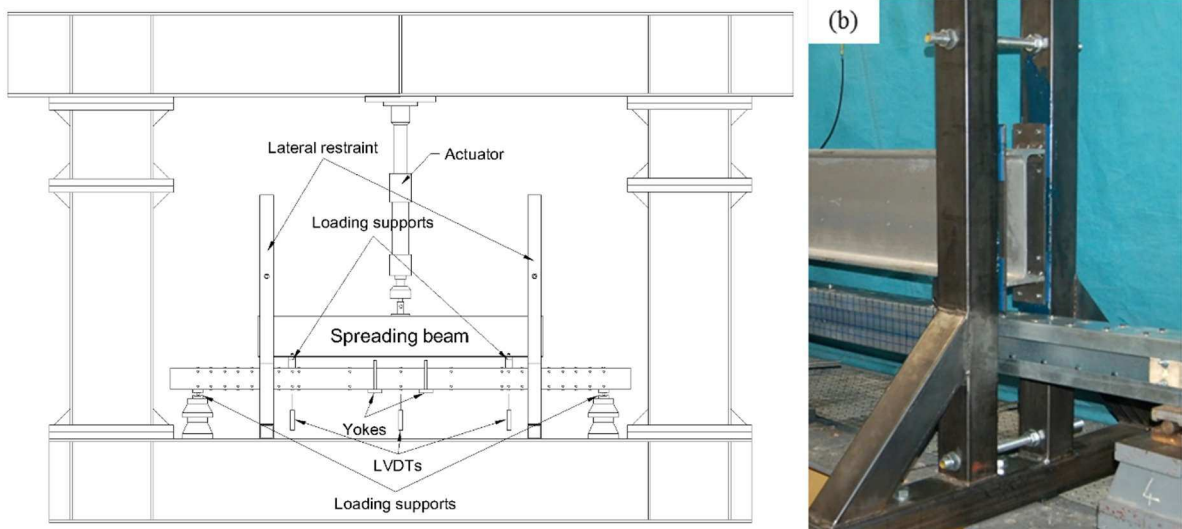


Fig. 13. a) Four-point bending test rig; **b)** Lateral support system

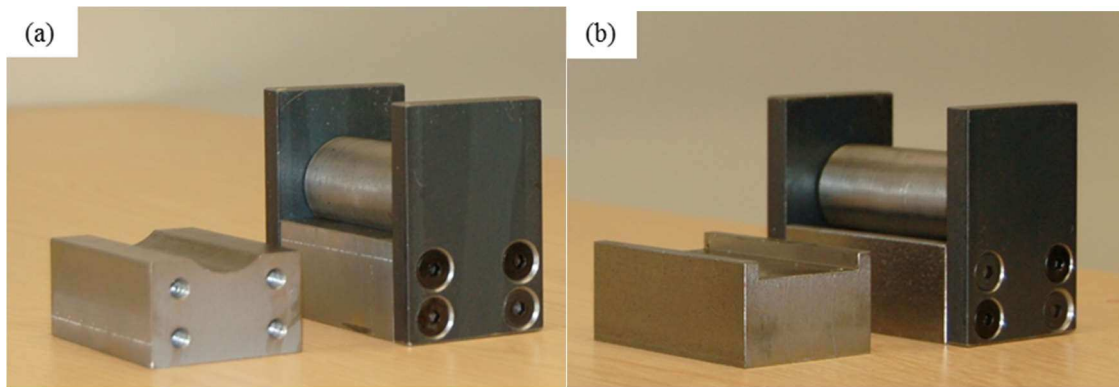


Fig. 14. a) Loading devices: a) Pin support; **b)** Loading devices: b) Roller support

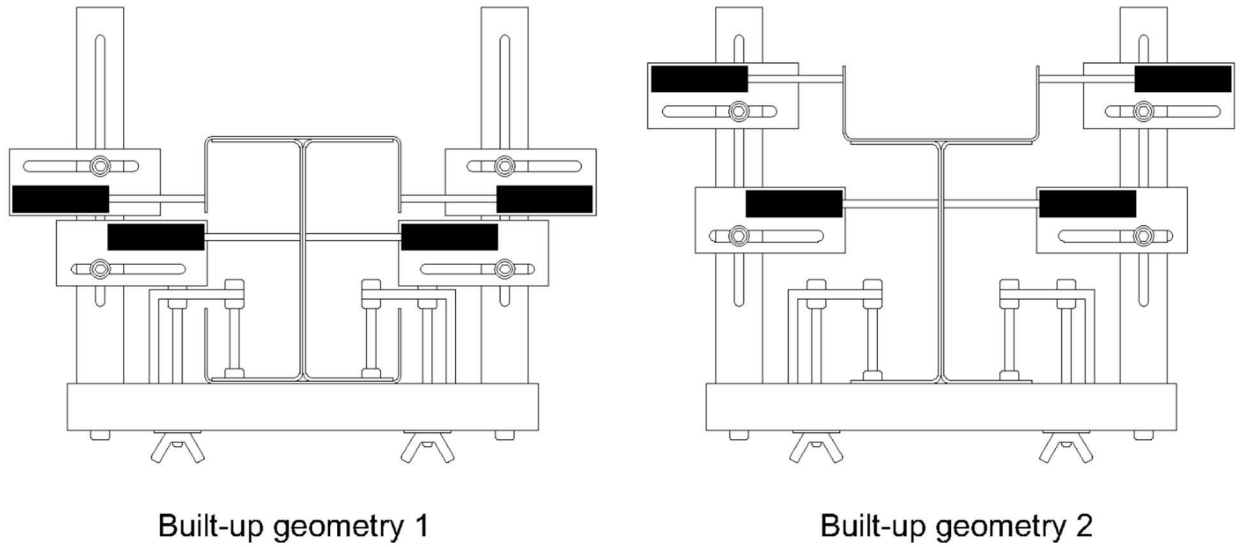


Fig. 15. Potentiometer lay-out within the cross-section

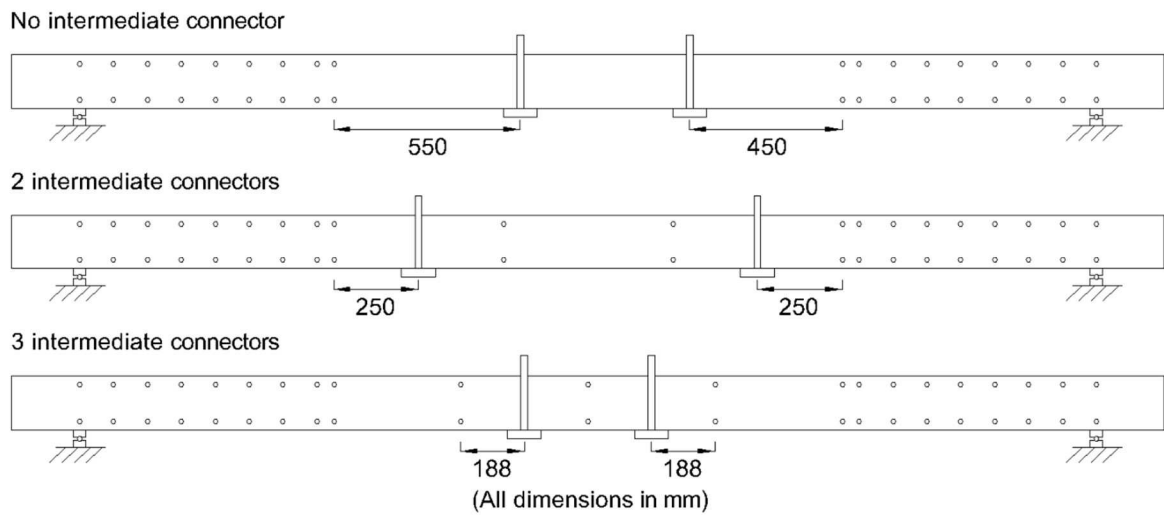


Fig. 16. Location of the potentiometers along the test specimens

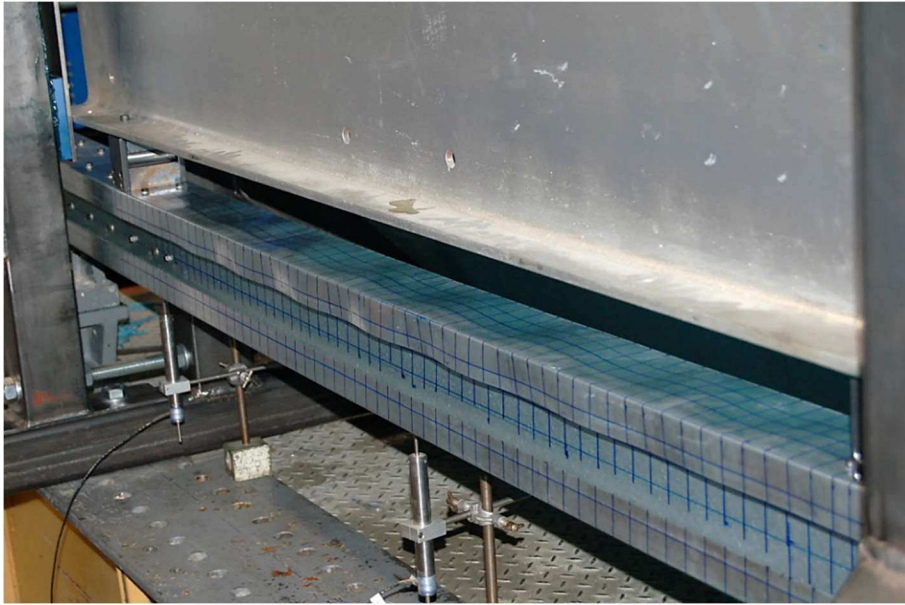


Fig. 17. Local buckling pattern (specimen B1-0b)

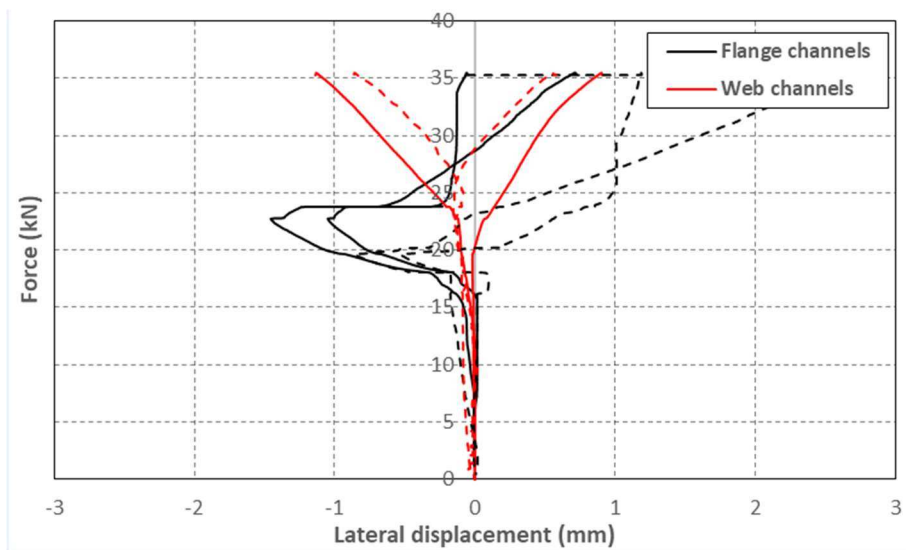


Fig. 18. Axial load vs lateral displacements (B1-3a)

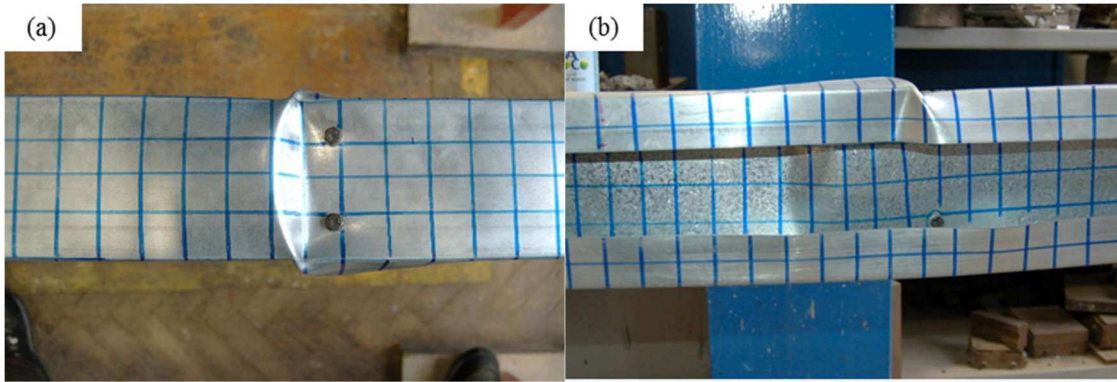


Fig. 19. a) Yield line mechanism in B1-2a: a) Top channel; **b)** Channels comprising the web



Fig. 20. Asymmetric yield line mechanism in built-up specimen B1-2b

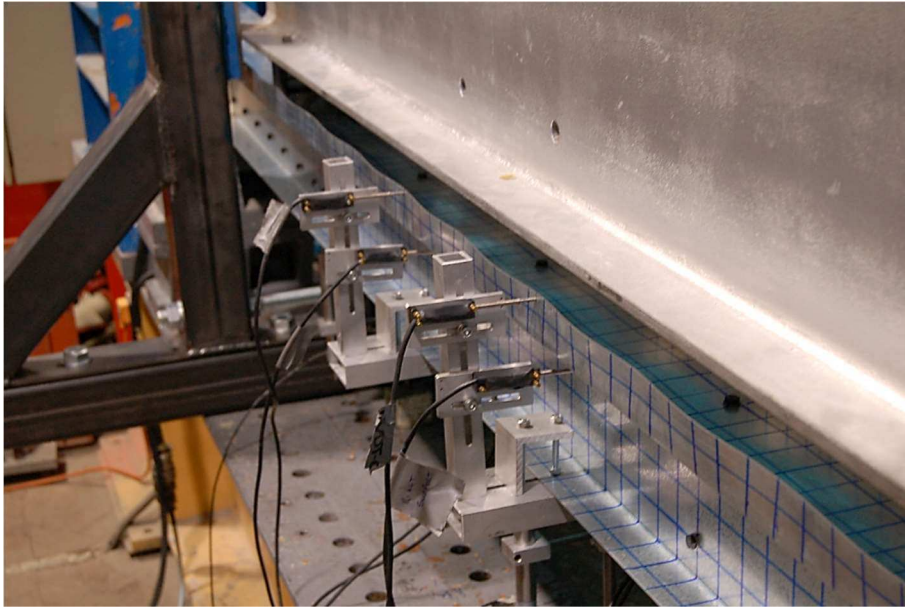


Fig. 21. Local buckling pattern (specimen B2-3a)

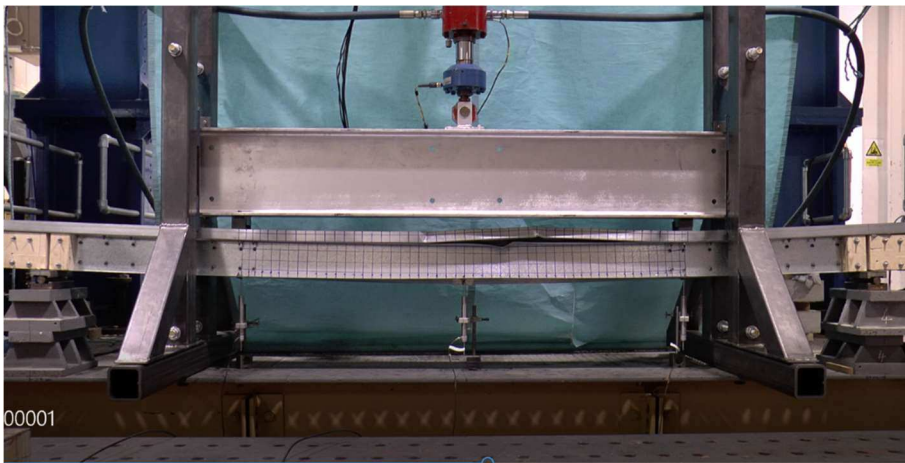


Fig. 22. Flexural-torsional deformations in specimen B2-0a, pictured after the peak load



Fig. 23. Flexural-torsional deformations in specimen B2-0b, pictured after the peak load

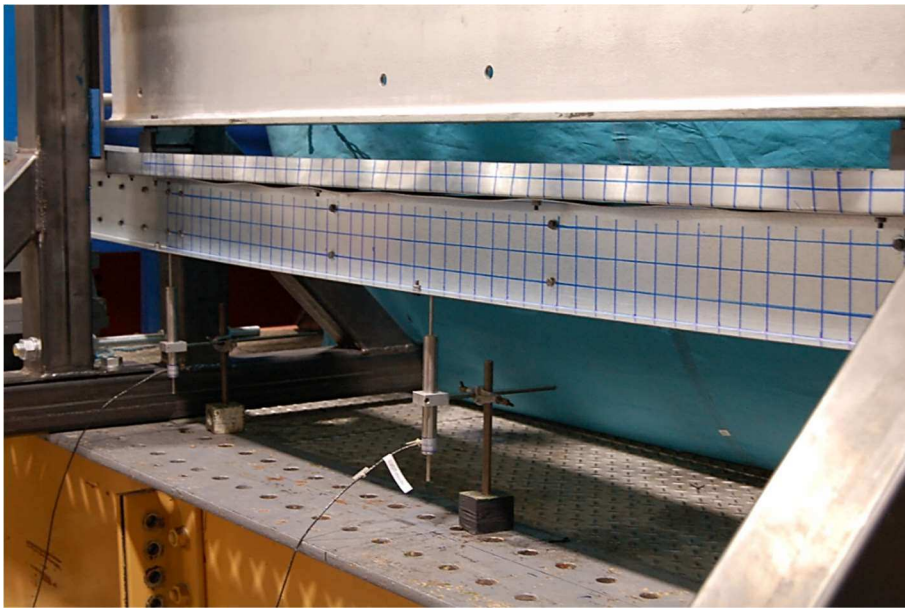


Fig. 24. Local buckling pattern in specimen B2-2b

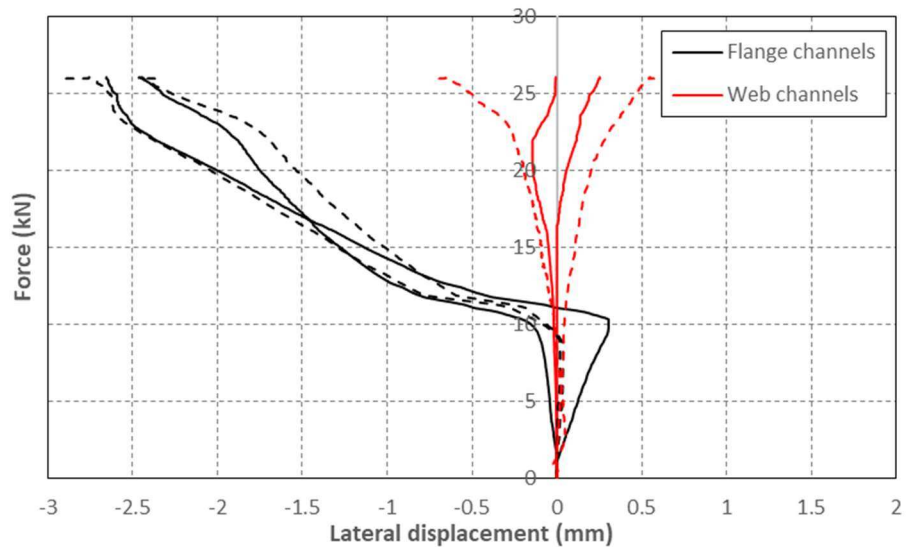


Fig. 25. Axial load vs lateral displacements of B2-3a

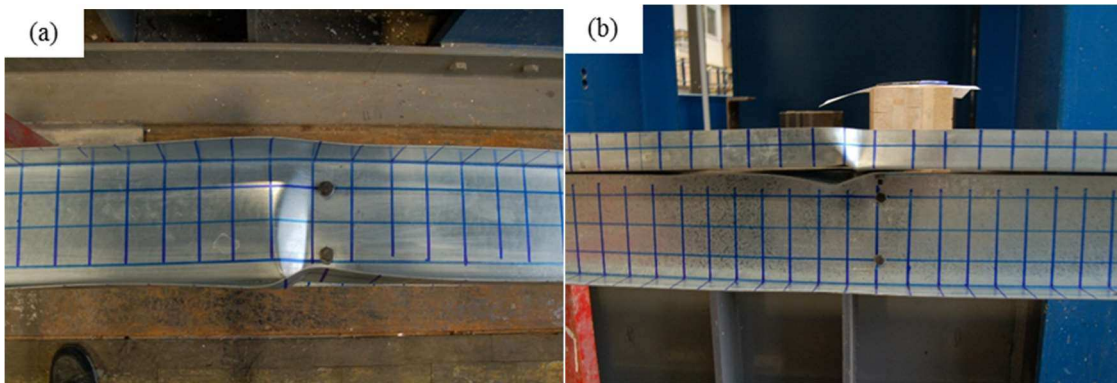


Fig. 26. a) Yield line mechanism in B2-2a: a) Top channel; b) Channels comprising the web

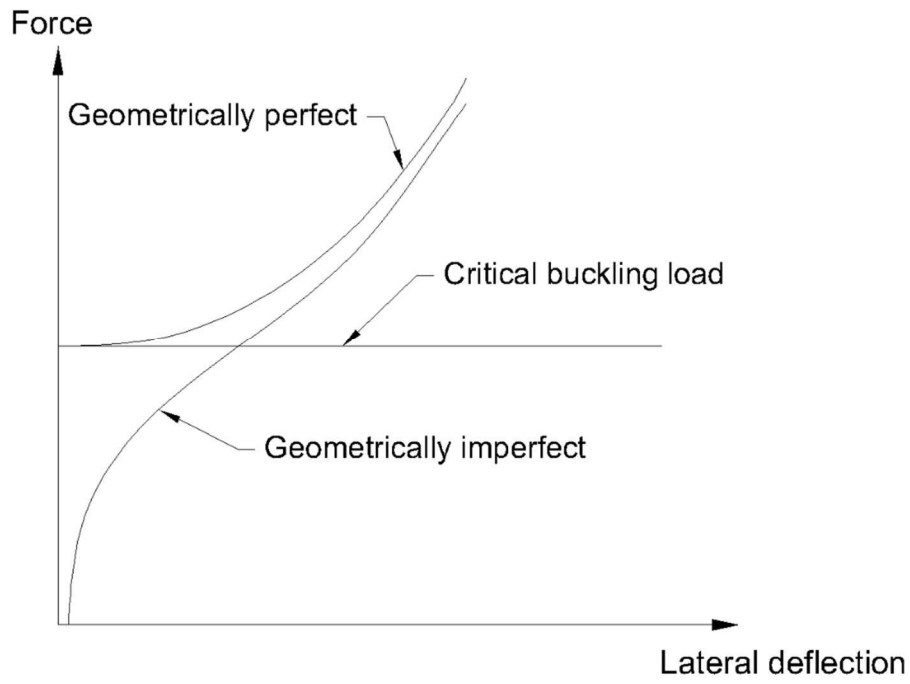


Fig. 27. Local buckling out-of-plane deformations

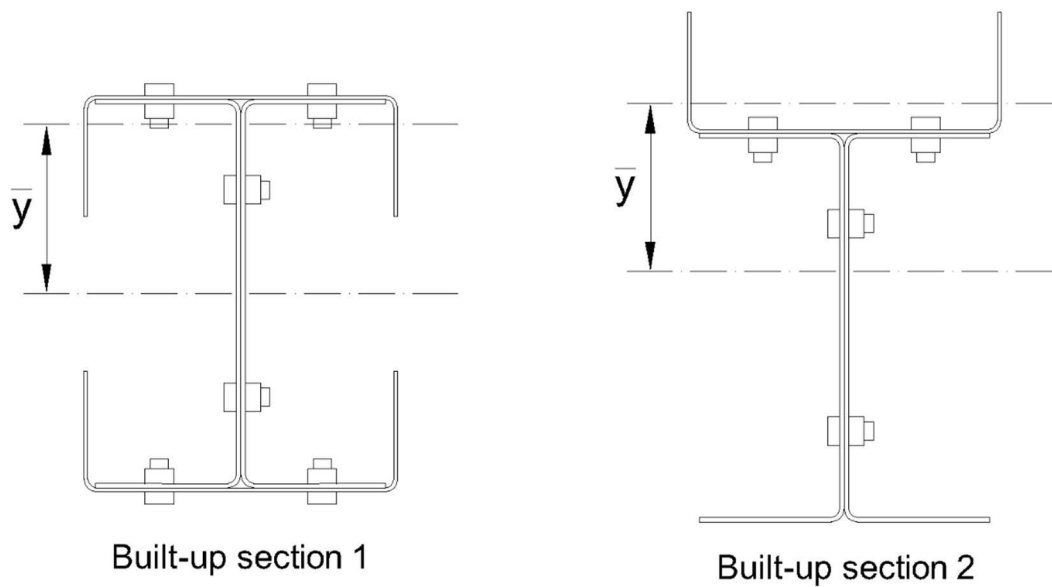


Fig. 28. Distance between the centroid of the top channel and the centroid of the built-up cross-section

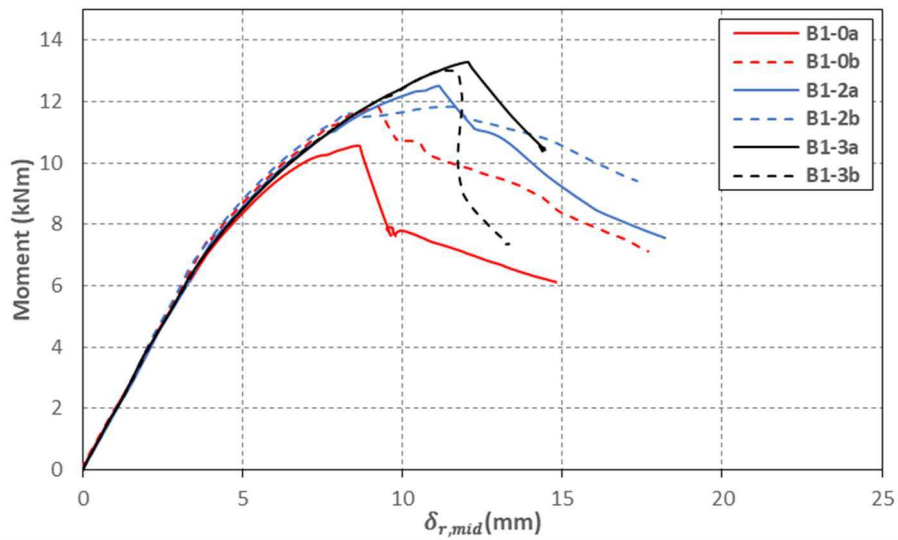


Fig. 29. Moment vs relative deflection at mid-span for specimens with geometry 1

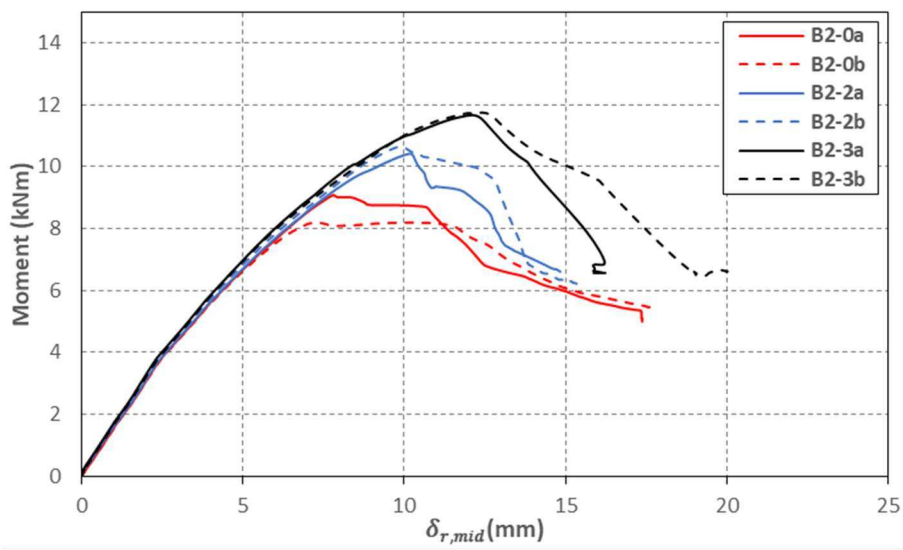


Fig. 30. Moment vs relative deflection at mid-span for specimens with geometry 2